Fatty acid monolayers on randomly nanostructured inorganic surfaces: Interplay of wettability, chemistry and topography

Mathieu Beauvais [a], *Irma Liascukiene* [b, †], *Alain M. Jonas* [c], *Jessem Landoulsi* [b, *]

[a] *Alcatel-Lucent Bell Labs France, 7 route de Villejust, 91620 Nozay, France*

[b] *Sorbonne Université, CNRS, Laboratoire de Réactivité de Surface, 4 place Jussieu, F-75005, Paris, France.*

[c] *Institute of Condensed Matter and Nanosciences, Bio & Soft Matter, Université catholique de Louvain, Croix du Sud 1 (L7.04.01), 1348, Louvain-la-Neuve, Belgium*

***Corresponding Author:** jessem.landoulsi@sorbonne-universite.fr

†Present addresses: Laboratoire de Physique de La Matière Condensée, Ecole Polytechnique, CNRS, IP Paris, 91128, Palaiseau, France

Abstract

Understanding the wetting properties of chemically-modified inorganic surfaces with random nanoscale topography is of fundamental importance for diverse applications. This issue has hitherto continuously been the subject of considerable controversies. Herein, we report a thorough investigation of the wettability-topography-chemistry balance for a surface with random nanoscale topography, the main challenge being decoupling topography from surface chemistry. For this purpose, we use a superficially nanostructured aluminum substrate chemically modified by fatty acid monolayers. From AFM data, we extract a variety of parameters describing the surface topography by means of variogram calculations, a method originally developed by geo-statists to explore large surfaces. Moreover, by using a power transform approach, we establish a consistent relationship relating wettability, topography and surface chemistry. Interestingly, we demonstrate that the water contact angle comprises a contribution due to the surface composition, originating from hydrophilization through alkyl chains, and a contribution due to the surface topography. This model is valid in the Wenzel region, and may suggest ways to tune the wetting properties of inorganic surfaces with nanoscale stochastic topographies.

1. Introduction

The topography of inorganic solid surfaces, typically metals, oxides and bioceramics, is a key parameter influencing the properties of materials and their performances, and is particularly important in coating technologies for the control of interactions with biological systems.[1, 2, 3, 4, 5, 6, 7] Owing to the remarkable progresses gained in nanosciences and nanotechnologies, many studies have reported the interest of controlling this parameter at the nanoscale to achieve and/or improve specific properties, especially in applications where the materials are used in wet conditions (adhesion, biocompatibility, water repellency, etc). In these applications, the surface of materials is frequently chemically modified with the aim to modify the physicochemical properties (hydrophobicity, electrical charge, solvation), which control the interactions with the surrounding entities. However, the effect of nanoscale topographies has hitherto continuously been the subject of considerable controversies. The origin of the main discrepancies reported in the literature may be explained by three key considerations. First, the notion of "nanoscale topography" includes a wide range of dimensions (from a few nanometers to hundreds of nanometers) and various morphological shapes and characteristics (randomly *vs* regularly rough surfaces), which complicate attempts to establish a general trend. Second, in many situations of practical relevance, surface roughening is accompanied by deliberate or non-controlled chemical changes so that the "roughness" parameter is not the only factor that has to be taken into account. Indeed, the common strategies used to control rough surface topographies at the nanoscale consist of physical processes based on lithography and physical vapor deposition techniques, [8] chemical processes, including etching, oxidation, etc, [9] and self-assembly of nano-objects. [10] Among all these procedures, only few techniques may lead to successful roughening with almost homogenous chemical composition, such as supersonic cluster beam deposition (SCBD) [11] and glancing angle deposition (GLAD). [12, 13] Accordingly, decoupling topography from surface chemistry remains experimentally rare. [14, 15, 16] Third, and

more decisively, the choice of the relevant parameters, which provide a quantitative description of the surface morphology is not obvious. In situations with common occurrence, surfaces of metals and oxides exhibit random topographies, which may be fully described by a n-point height probability distribution $p_n(\{(x_i,y_i)\}_{i=1\ldots n};\{z_i\}_{i=1\ldots n})$ such that $p_n.\mathrm{d}z_1\ldots\mathrm{d}z_n$ gives the probability that the heights z_n of the surface at n points of lateral coordinates (x_n,y_n) are simultaneously comprised between z_i and $z_i+\mathrm{d}z_i$, respectively. A complete description of the surface is obtained when n is very large; however, for practical purposes, most studies are limited to the cases of n=1 or 2, leading to the definition of two types of roughness parameters. The first type is related to p_1, the probability distribution of heights (amplitudes), whose second moment is the square of the root-mean-square roughness; other parameters, *e.g.* higher moments, can also be given to provide a more accurate description of the shape of p_1.[17] The second type is associated with p_2, which correlates the height at a given position to the one at another position; it is thus related to the spacing between topographical irregularities (lateral wavelength). While the first group parameters, *e.g.* root-mean square roughness, is only sensitive to the height differences (out-of-plane), the second group contains information on the horizontal or lateral range fluctuations (in-plane). The main functions providing direct lateral information are the power spectral density (PSD) and the height-height autocorrelation function, which both derive from Fourier transformation of the height profile, but other transforms have been also reported in the literature (see [18] and references therein).

This paper focuses on the surface characteristics of an aluminum substrate exhibiting nanoscale topography modified with fatty acid (FA) molecules. For this purpose, the inter-connection between wettability-chemistry-topography is thoroughly examined. The nanoscale topographies of planar surfaces may be conveniently characterized by atomic force microscopy (AFM). The main advantage of this technique lies in the possibility to probe almost all types of planar surfaces in a wide range of media. More importantly, it is the most relevant technique,

which provides direct measurements on nanoscale surface topographies, [19, 20, 21] even though its accuracy remains dependent on the dimensions of the tip. The use of AFM data to provide quantitative roughness parameters has been the subject of a vast literature. On inorganic solids, this approach has been employed to describe the characteristics of surface topographies for many purposes, such as to understand the mechanisms controlling surface growth,[12, 13] or to evaluate the impact of roughness on wetting properties.[22] In the present study, roughness parameters are determined by exploring AFM data following a statistical approach based on variogram calculations. This approach was initially developed by geostatists to provide quantitative description of natural variables in large surfaces of high complexity, such as soil porosity and permeability, concentration of pollutants, mineralization domains in ore deposits, etc. [23, 24] The roughness parameters extracted from variogram calculations are compared to those obtained by power spectral density, an approach broadly used for the characterization of nanostructured surfaces. By exploring different roughness parameters, a particular attention is dedicated to the impact of the self-assembled FA monolayers on the balance wettability-chemistry-topography.

2. Experimental section

2.1. Materials

Polycrystalline aluminum wafers (specimens of ~1 cm^2 surface area cut from a 2-mm thick plate, Al 99.99%, GoodFellow, France) were used in this study. Fatty acids (≥ 99.99%,), including stearic (SA), oleic (OA), linolenic (LA), lauric (LrA) and caprylic (CA) acids, heptane (HPLC grade, ≥99%) were purchased from Sigma-Aldrich (France) and used without further purification.

2.2. Surface modification

A stochastic roughness of aluminum surfaces was induced at the nanoscale by hydrothermal treatment performed in ultrapure water (MilliQ, Millipore, France), resulting in a superficial

hydroxylation of the surface, as described elsewhere. [25] Adsorption of fatty acids on the nanostructured aluminum substrate was carried out following the procedure described previously.[26] Briefly, samples were placed in glass Petri dishes containing the solution of dissolved FA in heptane at a concentration of 10 mmol/L, and incubated for 1 h with gentle stirring. The samples were then immersed in a solution of pure heptane for 5 min for rinsing, dried under nitrogen gas flow and used immediately. For each FA-modified surface, two to four independent sets of samples were analyzed to check the reproducibility (see the list of samples given in Table S1, Supporting information).

2.3. Atomic force microscopy (AFM)

AFM images were recorded using a commercial AFM (NanoScope VIII MultiMode AFM, Bruker NanoInc- Nano Surfaces Division, Santa Barbara, CA.). The substrates were fixed on a steel sample puck using a small piece of adhesive tape. Images were recorded in air at room temperature (~22°C). AFM experiments were performed using peak force tapping (PFT) mode, as detailed elsewhere.[27] In this mode, the z-piezo is modulated far below the cantilever resonance frequency (2 kHz), with an amplitude of about 120 nm. Oxide-sharpened microfabricated Si_3N_4 cantilevers were used (Bruker NanoInc- Nano Surfaces Division, Santa Barbara, CA.). The spring constants of the cantilevers were measured using the thermal noise method, yielding values of 0.5 (±0.05) N/m and the curvature radius of silicon nitride tips was about 3 nm (manufacturer specification).

2.4. Water contact angle (WCA)

Static water contact angles were measured at room temperature using the sessile drop method and image analysis of the drop profile. The apparatus (Krüss, Germany) is equipped with CCD camera and an image analysis processor. The ultrapure water droplet volume had a 1 µL volume and the contact angle was measured about 3s after the drop was deposited on the sample surface. For each sample, the reported value is the average of the results obtained with 3 droplets.

2.5. Polarization-modulation infrared reflection absorption spectroscopy (PM-IRRAS)

PM-IRRAS is a non-destructive surface characterization technique, which is convenient for probing thin films deposited on metal substrates. This method utilizes light, which is continually alternated between p- and s- polarizations by means of a photo-elastic modulator (PEM). In the condition of near specular reflection, s-polarization and the main component of p-polarization are parallel and perpendicular to the sample surface, respectively. The p-polarization includes information about the adsorbed compounds on the surface and in the gas phase, whereas the s-polarization includes information about only the gas phase. The PM-IRRAS spectrum is thus obtained by dividing the measured difference reflectivity (R_p - R_s) by the sum reflectivity (R_p + R_s), where R_p and R_s are the intensity of the p-polarized and s-polarized component of the radiation, respectively. PM-IRRAS spectra were recorded on a commercial Nexus spectrometer (Thermo-Scientific, France). The external beam was focused on the sample with a mirror, at an optimal incident angle of 80°. A ZnSe grid polarizer and a ZnSe PEM, modulating the incident beam between p- and s-polarizations (HINDS Instruments, PEM 90, modulation frequency = 37 kHz), were placed prior to the sample. The light reflected at the sample was then focused onto a nitrogen-cooled MCT detector. All the spectra presented were obtained from the sum of 128 scans and the band positions are estimated to have a 8 cm^{-1} resolution.

3. Statistical analysis of AFM images

All the calculations detailed below were performed on AFM images by using the AFM R library available on the R CRAN repository. [28]

3.1. Areal dependence of the roughness of self-affine surfaces

The fractal formalism has been extensively used to describe rough surfaces at different scales, including surfaces with nanoscale topographies.[29, 30, 31, 32] For a statistical description of surface roughness, let us consider a conventional three-dimensional coordinate system arranged so that the (x,y) plane corresponds to the average plane of the surface. The fluctuations perpendicular

to the surface plane may be described by a statistical variable, the height function *h(x,y)*. From a mathematical point of view, surface roughness is considered as self-affine if it remains invariant under anisotropic affine transformations of the form given below:

$$(x,y) \rightarrow (\lambda x, \lambda y),$$

$$h(x,y) \approx \lambda^{\zeta} h(\lambda x, \lambda y) \qquad \text{for } x,y \neq 0 \tag{1}$$

where λ is the scaling factor and ζ is the roughness exponent, which is considered as a quantification of the roughness changes with the length scale (lateral dimension).[33] It is worth noting that the sign "≈" is used because Eq. 1 is only valid in a stochastic sense.[34]

The roughness measurement depends on the length scale over which it is performed. A standard measure of roughness at a given length scale L is the root-mean-square roughness of the height differences over a two-dimensional surface of area L^2 :

$$w(L) = \left(\frac{1}{L^2}\int_0^L \int_0^L [h(x,y) - \bar{h}]^2 dx dy\right)^{\frac{1}{2}} \tag{2}$$

where the mean height is given by $\bar{h} = \frac{1}{L^2}\int_0^L \int_0^L h(x,y) dx\, dy$. For self-affine surfaces obeying Eq. 1, it is shown that the root-mean-square of the height differences scales as :

$$w(L) \approx L^{-\zeta} \tag{3}$$

For real self-affine surfaces, w saturates at large length scales L, *i.e.*, there is a lateral cutoff length, L_c, from which $w(L) \approx w_{sat}$ (constant) if $L >> L_c$. This cutoff length, also called crossover length, corresponds to the length scale below which the height fluctuations of the surface remain laterally correlated.

Accordingly, a self-affine surface, which obeys the anisotropic scale invariance (Eq. 1), may be characterized by three parameters only: (i) the saturation value of the roughness, which is an amplitude (vertical) parameter, (ii) the roughness exponent ζ, which is related to the jaggedness of the surface, and (iii) the crossover length, which is a lateral spatial parameter. These three parameters may be extracted from *w(L) vs L* plots.

Another parameter, which may be also computed by self-affine models is the fractal dimension, D_F. Originally, the fractal dimension is an invariant-scale parameter, which characterizes self-similar objects, *i.e.*, objects invariant under isotropic scale transformations. For self-affine surfaces, however, invariance is only exhibited for anisotropic transformations. D_F is scaling-independent, in contrast to the roughness parameters described above which are scale-dependent, *i.e.*, which provide a direct information on the roughness changes as a function of the distance along the surface. The estimation of the fractal dimension may be performed using a variety of methods, [35] most of them being difficult to apply on planar surfaces with nanoscale roughness.

3.2. Power spectral density (PSD)

The 2D-PSD of the topography function $h(x,y)$ sampled over a set of discrete locations (x_n,y_m) can be calculated by a 2-dimensional Discrete Fast Fourier Transform routine $\Im$ [36]:

$$PSD\ (u_m, v_n) = \frac{A}{(MN)^2} |\mathcal{F}\{h(x_m, y_n)\}|^2 \quad (4)$$

where $\Im$ is the 2-dimensional Discrete Fast Fourier Transform routine; x,y the spatial coordinates, u, v the reciprocal coordinates (or spatial frequencies), A the surface of the sample, and M and N are the total numbers of sample points in the x and y directions, respectively.

From the Wiener-Khintchine theorem, the PSD bidimensionally-integrated over spatial frequencies ranging from $\rho_{mn}=1/l_{mn}$ to infinity yields the square of the root-mean-square roughness measured over an area of size l_{mn}^2, $w^2(l_{mn})$. [37] For an image acquired with a sampling step of Δx and Δy in the x and y spatial directions, respectively, the root-mean-square roughness at a given length scale l_{mn} can thus be obtained from the discrete PSD as follows:

$$w^2(l_{mn}) = \frac{1}{A}\sum_{\rho\in[\rho_{min},\rho_{max}]} PSD(\rho) \quad (5)$$

with ρ_{max} the maximum spatial frequency (Nyquist frequency) defined as the minimum spatial frequency among $\frac{1}{2\Delta x}$ and $\frac{1}{2\Delta y}$.

Obviously, the limit of w for very large areas can be directly calculated from the 2D-PSD as follows:

$$w_{sat}^2 = \frac{1}{A}\sum_{\rho\in[0,\rho_{max}]} PSD(\rho) \quad (6)$$

3.3. Empirical and theoretical variogram calculation

Empirical variogram calculations have been broadly used by geo-statisticians to explore large surfaces and interpolating experimental data with the aim to predict the distribution and spread of compounds (pollutants, minerals, etc.).[38, 39] The use of variograms is related to the probability distribution p_2 defined above, and is based on the fundamental idea that two spatially closed observations should be more similar than two observations that are not so close. Geo-statisticians have used empirical variograms to evaluate the mean and the variance of points of measurements taken two by two. As only two measurements are made to evaluate the mean and variance, an additional hypothesis of second order stationarity is considered. The second order stationarity implies that it is possible to use all the pairs of points separated by a distance d (between x and $x+d$) to evaluate the mean and the variance.

In the present study, we adopted this approach to characterize the nanoscale surface topography. For this purpose, the AFM image was treated as a two-dimensional set of data points with a topography function $h(x,y)$. The semi-variance, also known as the pair correlation function, is computed for all data without considering directions as follows:

$$\gamma(d) = \frac{1}{2N}\sum_{(i,j)=1}^{N}[\,h(r_i) - h(r_j)]^2 \quad (7)$$

with N the number of distinct pairs of sample points at locations r_i and r_j such that the norm of the vector connecting r_i to r_j is within $[d, d + \varepsilon]$ with ε the distance intervals into which data point pairs are grouped.

In the present study, the variance was calculated in several directions for isotropy assessment.[40] Only samples the surface of which exhibit isotropic feature are considered. Pairs of sample

points are grouped for semi-variance estimates depending on the direction θ of the pairs of sample points. The semi-variance is calculated as follows:

$$\gamma_\theta(d) = \frac{1}{2N(\theta)} \sum_{(i,j)=1}^{N(\theta)} [\, h(r_i) - h(r_j)]^2 \quad (8)$$

with θ the angle between the vector connecting points *i* and *j* and the vertical axis (perpendicular to the surface plane).

Data from AFM images are spatially equally distributed, therefore, the calculation of semi-variograms does not require any pre-treatment. However, both sample isotropy and a normal distribution of heights is necessary for a robust estimation of the variogram.[41]

The calculation of theoretical variogram models are performed using the universal kriging method and evaluated with a cross validation of the model with both correlation between real and predicted heights and precision of heights prediction.

3.4. Estimation of fractal dimension

3.4.1. Power spectrum method

Data obtained from power spectrum treatment, *e.g.* PSD, may be used for the estimation of fractal dimensions.[42] The fractal dimension is estimated with:

$$D = \frac{7 - slope}{2} \quad (9)$$

where *slope* is the absolute value of the slope determined using a linear least square regression on the log-log 2D-PSD.

3.4.2. Variogram method

The variogram method has been also used for the determination of fractal dimensions of surfaces of geophysical interest.[42] This method is considered to be rigorous and easy to implement when dealing with self-affine surfaces.[43]

For isotropic and Gaussian fields, the fractal index and the fractal dimension can be calculated with a linear regression at small lags of the experimental variogram in the log-log space [43]:

$$\log\{\gamma(d)\} \approx \log(2c) + \alpha \log(\|d\|) + o(1) \quad (10)$$

with α the fractal index and c the topothesy.

The estimation of the fractal dimension D is then calculated from the estimation of the fractal index α with [43] :

$$D = d + 1 - \frac{1}{2}\alpha \quad (11)$$

4. Results and discussion

4.1. General characteristics of the nanostructured aluminum *surfaces*

The hydrothermal treatment performed here on the aluminum samples, also called hydroxylation, is a well-known procedure, which converts Al_2O_3 into pseudo-bohemite.[44] On flat Al substrates (called *Al*), this treatment leads to the modification of the native oxide layer, initially present on the aluminum surface (probably poorly crystalline alumina), into a AlOOH compounds, presumably pseudo-bohemite (called *Al-nano*). This reaction is supported by PM-IRRAS analyses. [25, 45] Interestingly, this chemical transformation is accompanied by a drastic change of the surface morphology as shown in Figures 1A and B. While the hydrothermal procedure has been thoroughly used for Al-based materials, its effect on the surface morphology of planar substrate is still limited to few reports.[14, 25, 26, 27] The surface exhibits elongated nanostructures densely and randomly distributed on the surface, and nanoporous domains with different sizes along and perpendicular to the surface plane. The dimensions of these nanostructures may be tuned by further treatments, *e.g.* in H_2O_2 solution (*Al-nano_Ox*, Figure 1C), but their chemical composition did not change.[27] The surface "viewed" by AFM may not fully describe the topography of the nanostructured aluminum surface. This may be due to a convolution effect associated to the geometry and the dimensions of the tip. More importantly, the difficulty to probe this superficial hydroxylated layer is inherent to the complexity of its own structure: it may include nanoporous domains with polydisperse dimensions and different

degree of confinement, which may not be wholly accessible for a scanning probe microscopy technique. AFM provide, thus, a view of the nanostructured surface essentially including the exposed regions.

The self-assembly of fatty acid on the nanostructured aluminum surface (*Al-nano*) led to slight evolution of the surface while the main topography remained unchanged (see AFM deflection images in Figures 1D and E). The main feature consists in the appearance of ordered nano-patterns, which are aligned following the axis of the elongated nanostructures and clearly discernable in the AFM deflection image (Figure 1F). PM-IRRAS analyses provide relevant information regarding the mechanism of interaction of FAs with the nanostructured surface (Figure 1G). Results showed the absence of a band in the 1700-1750 cm^{-1} region due to ν(C=O), which is clearly visible when molecules are "free" in solvent. This suggests the formation of coordinative bonds between carboxylate end groups of the fatty acids, the carboxyl moiety being deprotonated, and Al^{3+} ions on the *Al-nano* surface. The type of carboxylate coordination, terminal or bridging (between two Al^{3+} centers), monodentate or bidentate, etc, is however not demonstrated and requires further investigations. Importantly, these results suggest the formation of self-assembled monolayer of FA, which makes the surface hydrophobic (see insets in Figures 1D and E). The obtained FA-modified *Al-nano* samples are called *Al-nano_FA*.

The self-affinity of the different nanostructured surfaces was investigated using the formalism described above (*section 3.1.*). Figure 2A shows the plots of root-mean-square roughness (w) as a function of the length scale (L) for different samples (see Figure 2 caption). Results reveal the increase of w with L and the existence of a crossover length (L_c) after which the roughness saturates. The roughness obtained at the saturation, w_{sat}, was given by the plateau at large length scale values. The log-log plots (Figure S1, Supporting Information) shows that the root-mean-square roughness follows a power law, as expected from Eq. 3, for small length scales, i.e before reaching the saturation value, w_{sat}. Considering the experimental variability, the roughness

exponent values obtained on the studied samples are around 0.9 (Figure S1). This value is close to the one reported for vapor-deposited films,[12] even if its interest for deciphering the mechanism of surface growth is not obvious. These results show that the presence of FA monolayers on the nanostructured aluminum surfaces does not influence the roughness changes at small length scales.

The self-affine properties of the aluminum substrates were also investigated using the variance method. The procedure used for variogram calculation is described in Figure 3. For a given AFM image (Figure 3A), the condition of height normal distribution is required for variogram calculation (Figures 3B and C). The isotropy condition is checked by calculating, at least, four directional variograms (Figure 3D). This allows to average all experimental semi-variograms yielding an omni-directional semi-variogram. It is shown that the initial rate of increase of $\gamma(L)$ as a function of the length scale is the same in all directions (Figure 3D), suggesting an isotropy at the scale of the features. The variogram modeling allows two relevant parameters related to surface roughness to be extracted. The first is called "*range*" and is interpreted as the maximum distance at which two sample points are still correlated. The second is called "*sill*" and corresponds to the saturation level of the semi-variance at distance higher than the range. Variogram modeling was performed using the universal kriging method from the empirical variogram, as described above (see *section 3.3.*), and evaluated by cross validation. For this purpose, about 3.5% of sample points are randomly selected to perform the modeling for a given empirical variogram model. The complementary points are used to evaluate the quality of the model by comparing the predicted values with the real values of the image (Figure 3E and F). The quality of the model chosen is evaluated by means of two variables (Supporting information, *section 2.2*): *Precision* variable (the sum of the square of differences between predicted and real values of heights) and *Correlation* variable (the correlation between the predicted and real values of heights).

In the present study, by evaluating eighteen empirical models on a set of sixteen FA-modified aluminum samples, it appeared that the Pentaspherical variogram model is the most suitable:

$$\gamma(d) = \frac{15d}{8a} - \frac{5}{4}\left(\frac{d}{a}\right)^3 + \frac{3}{8}\left(\frac{d}{a}\right)^5, 0 \le d \le a \quad (12)$$

and

$$\gamma(d) = 1, d>a \quad (13)$$

where *a* is the *range*.

The *range* and *sill* values extracted from the variance modeling are reported in Table S1 (Supporting information) for different *Al-nano_FA* samples. The results given in Figure 2B show that *sill*, thus the variance, is very low for flat aluminum substrate, suggesting that the height values are very close to the mean value and hence to each other. By contrast, on *Al-nano* samples as such or further conditioned in H_2O_2 solution (*Al-nano_Ox*) or modified with FA (*Al-nano_FA)*, *sill* is significantly higher, indicating that the heights are very spread out around the mean value and from each other.

All the roughness parameters obtained from *w(L) vs L* and γ(L) vs *L* plots are summarized in Table S1 (Supporting information). The relationship between parameters extracted via the PSD method or variogram calculations is given in Figure 4. Actually, *sill* is equal to the variance of the random topography function *h*(x,y), when measured over a spatial range larger than the correlation range [46] :

$$sill = \frac{1}{L^2}\sum[h(x,y) - \bar{h}]^2 \quad (14)$$

The variance measures how far the heights *h*(*x*,*y*) of a sample are spread out. From equation (2), the square-root of the variance of heights of the sample is the total root-mean-square roughness of the sample. Thus, the square-root of the *sill* is the total root-mean-square roughness of the sample:

$$w(L) = sill^{0.5} \quad (15)$$

The plot of w_{sat} *vs* $sill^{0.5}$ gives a slope close to 1, indicating a fairly 1:1 relationship in agreement with Eq. 15 (Figure 4A). This suggests the consistency of data extracted, independently, from PSD and variogram calculations. In the same way, a linear relationship between L_c and range was obtained (Figure 4B). Fractal dimensions determined through the PSD method and variogram calculations, using Eq. 9 and Eq. 11, respectively, also show consistent values clustered around ca. 2.1 (Figure 4C). The consistency of parameters extracted from the two methods suggest that variogram calculations are, thus, promising for the characterization of surfaces with random nanoscale topographies.

4.2. Wettability-chemistry-topography balance

The origin of wetting properties of the *Al-nano_FA* surfaces may be scrutinized by examining correlations between (i) parameters due to the amount of self-assembled FAs in the adsorbed phase, (ii) parameters describing the surface topography, and the (iii) apparent water contact angle (θ_w). The balance wettability-chemistry-topography is thoroughly examined for all FA-modified aluminum samples (*Al-nano_FA*), which exhibit θ_w values ranging from ca. 118 to ca. 133° (Table S5, Supporting information). First, these samples all exhibit a controlled (in the sense of reproducible) random nanoscale topography. Second, they are all chemically-modified with FAs so that the interference with adventitious organic contamination, largely present on bare inorganic solids, [47] is limited. The range of θ_w values, even narrow, is relevant to make tentative of decoupling topography from surface chemistry for these hydrophobic rough surfaces. It is noteworthy that *Al-nano_FA* with lower θ_w values can be obtained by performing a partial desorption and/or degradation of adsorbed FAs.[26] These surfaces are, however, difficult to characterize because of their heterogenous chemical composition, and the lack of information regarding the localization of FA molecules (exposed the outermost part of the surface or confined in deeper regions).

The chemical composition of *Al-nano_FA* surfaces may be obtained by exploring vibrational band from PM-IRRAS spectra, which is characteristic of FA molecules. This non-destructive physicochemical analysis is highly sensitive for the characterization of thin films deposited on metal substrates, including molecular adlayers.[48] Regarding the studied system, PM-IRRAS probes the superficial hydroxylated layer in its entirety, thus, the whole adsorbed FA molecules. The integrated intensity (*i.e.* the area of the band) of the C-H stretching band due to the alkyl chains ($A_{\nu(C\text{-}H)}$) was thus used. It must be kept in mind that Aν(C-H) measured by PM-IRRAS is different to the surface concentration required in the Cassie relation. It corresponds to an average value over the depth scale probed by PM-IRRAS, expected to be the whole hydroxylated layer. Owing to the presumable presence of nonporous domains with high polydispersity, it is likely that a significant amount of adsorbed FAs is not "concerned" by the wetting phenomena. On planar surfaces, the water contact angle is expected to be governed by short-range interaction between water molecules and the "ideal" solid surface. The situation is, however, much more difficult for the studied system. If we accept the idea that FA molecules are completely covering the AlOOH surface, it is difficult to identify the "chemically relevant region" involved in wetting properties. Accordingly, an average value over the probed depth could be helpful as a variable describing surface chemistry.

The roughness is described using the different parameters extracted from AFM images using variogram calculations, namely *sill* and *range*. Multiple linear regression was used to examine the impacts of these variables on the variations of θ_w (see *section 3* in Supporting information for more details).

Several models for the prediction of the wettability, θ_w, including all or part of the transformed variables, *i.e.* $A_{\nu(C\text{-}H)}$ for surface chemistry and *sill* and *range* for surface topography, were tested and evaluated using the Akaike information criterion (AIC),[49] by means of a stepwise

algorithm (*section 3.2*, Supporting information). Only $A_{\nu(C\text{-}H)}$ and *range* transformed variables were selected by the algorithm, yielding the following model for θ_w prediction:

$$\theta_w = 74.04 + 69.91 \times log\left(10 \times A_{\nu(C-H)}\right) + 252200 \times \frac{1}{range^{2.15}} \quad (16)$$

This model provides a clear picture regarding the dependence of wettability with chemistry and topography for the nanostructured FA-modified surfaces. The model clearly shows that the water contact angle, θ_w, includes (i) one contribution due to the surface composition (hydrophobization through alkyl chains) and (ii) one contribution due to the surface topography. Figure 5 presents each contribution in a separated graph. Both values of boxed variables (open squares) and the theoretical line corresponding to the mathematical function used for the variable transformation (Box-Cox transformation, see Supporting information for more details) are shown. These graphs show the impact of the variation of each variable, $A_{\nu(C\text{-}H)}$ and *range*, on the resulting θ_w. Looking at Figure 5, one could conclude that each parameter, chemistry and topography, influences the surface wettability to a different degree. It is shown that surface chemistry induces a variation of about 20° in θ_w values (Figure 5A, left y-axis), while a change of the range (from 150 to 100 nm) induces a change on the contribution to θw (due to the range) that does not exceed 8° (Figure 5B, left y-axis). This trend may be due to the fact that in the studied system, *FA-Al_nano* samples have the same underlying substrate (*Al_nano*) and that the self-assembly of FAs did not considerably impact the surface topography. Importantly, it must be kept in mind that chemistry and topography are independent predictors, as discussed above. As a consequence, a combination of these parameters to use the balance of chemistry-topography to predict wettability would be, thus, relevant.

A broadly similar conclusion can be reached by considering the Wenzel equation, valid when the cavities of the surface are filled by the fluid,[50] as is the case here based on the moderately high values of contact angle. In this impregnation regime,

$$\cos\theta_w = r\cos\theta_f \quad (17)$$

In which θ_f is the contact angle that would be measured for a perfectly flat surface of identical chemical composition, and *r* the Wenzel roughness, *i.e.*, the ratio between the developed and projected areas of the surface. Here again, only two parameters determine the value of contact angle, one related to the surface chemistry (θ_f), one related to the surface topography (*r*). The Wenzel roughness can be directly obtained from AFM images by averaging the "local roughness" $\sqrt{1+(\frac{\partial h}{\partial x})^2+(\frac{\partial h}{\partial y})^2}$ over the sample surface.[51] Values are collected in Table S6 (Supporting information); they range from 1.41 to 1.55, which is a relatively small variation from sample to sample. From these values, θ_f values were computed for each sample according to Eq. (17) (Table S6). Samples with values of $A_{v(C\text{-}H)} < 0.35$ have $\theta_f \sim$ 108-110°, whereas samples with higher $A_{v(C\text{-}H)}$ values have $\theta_f \sim$ 116-118°, confirming the relation existing between surface chemistry ($A_{v(C\text{-}H)}$) and θ_f. However, the predictive power of Eq. (17) remains limited due to the morphological closeness of the samples, which can only be sorted in two groups based on θ_f. In contrast, the variogram-based approach as embodied in Eq. (16) provides a much finer analysis of the dependence of contact angle on surface chemistry and topography.

Figure 5 shows the impact that a variation of surface topography would have on wettability; for instance, a decrease of *range* leads to an increase of the water contact angle. This means that the more the surface is random the more it is hydrophobic. This trend is consistent with the fact that surfaces of shorter *range* exhibit a larger surface area, hence a larger Wenzel roughness. Our findings suggest that the proposed wettability-chemistry-topography balance is valid for all *Al-nano_FA* samples, i.e. with surfaces exhibiting a certain hydrophobicity. This is reflected by the term 74.04 in Eq. (16) and shown by the experimental θ_w values presented in Figure 5 (open circles), which are situated in the Wenzel regime region.

These results show that the variogram-based method is remarkably useful to extract relevant parameters describing the surface topography from AFM images. Moreover, the approach

adopted in the present study suggests a reliable way to examine the wettability-chemistry-topography balance for chemically-modified surface with random nanoscale topography. On the contrary, root-mean square roughness has been extensively used in the literature as the topographical variable to deal with interfacial processes in wet conditions. The weakness of this parameter lies on its insensitivity to lateral range fluctuations, *i.e.* in-plane, which are particularly important for surfaces with stochastic topographical features. In this respect, the Wenzel roughness is a better discriminator, but its integral nature somewhat blurs the details of the analysis of wetting compared to what was done here. Furthermore, despite the difficulties to fully characterize the surface chemistry and topography of the superficial hydroxylated layer, owing to its complex structure, the obtained results support the consistency of the variable used as predictors for wettability. Our results also provide guidelines for the control of wetting properties. For instance, increasing water contact angles may be achieved by decreasing the *range* (Eq. (16), Figure 5B), which can be easily obtained by tuning the mean size of surface nanostructures using different conditions of hydrothermal treatment, other chemical treatments (*e.g.* H_2O_2, Figure 1C), or a combination of the two treatments. In the context of biomaterials science, modulating wettability through topography, while controlling surface chemistry, would be an outstanding way to decipher protein adsorption behavior and cell response on nanostructured surfaces with fractal geometry. These surfaces are good candidates to overcome this challenge. Moreover, by adapting chemical procedures, the approach may be extended to other metallic materials of biological interest, including titanium and magnesium and their alloys.

5. Conclusion

In this article, the balance wettability-chemistry-topography was examined on a nanostructured aluminum surface with random topography, functionalized with a self-assembled monolayer made of fatty acids. Particular attention was given to the determination of variables describing

the topography of these surfaces from AFM images. Our results showed the possibility to extract relevant parameter using variogram-based calculations. Interestingly, it has been demonstrated, through a detailed model, that the water contact angle, θ_w, includes one contribution due to the surface composition and one contribution due to the surface topography. The approach detailed in this work to fully describe the surface properties of FA-modified randomly nanoscale rough inorganic substrates is straightforward and reproducible. Moreover, parameters extracted from AFM images provide practical information to finely tune the surface wettability of inorganic materials for broad applications. From a biomedical perspective, these investigations may pave the way to the design of new biomaterials with stochastic spatial organization of lipids to control subsequent interaction with biological molecules, as alternatives to micro-scaled regularly patterned surfaces. For instance, it would be interesting to assess to what extent the effects observed in the present study are applicable to proteins, and if wettability can be used as a "proxy variable" for protein affinity, correlated to it but easier to measure.

References

1. Liu, X.; Chu, P. K.; Ding, C. Surface nano-functionalization of biomaterials. *Materials Science and Engineering: R: Reports* **2010,** *70* (3), 275-302.
2. Paital, S. R.; Dahotre, N. B. Calcium phosphate coatings for bio-implant applications: Materials, performance factors, and methodologies. *Materials Science and Engineering: R: Reports* **2009,** *66* (1), 1-70.
3. Lord, M. S.; Foss, M.; Besenbacher, F. Influence of nanoscale surface topography on protein adsorption and cellular response. *Nano Today* **2010,** *5* (1), 66-78.
4. Park, J.; Bauer, S.; Schlegel, K. A.; Neukam, F. W.; von der Mark, K.; Schmuki, P. TiO2 Nanotube Surfaces: 15 nm—An Optimal Length Scale of Surface Topography for Cell Adhesion and Differentiation. *Small* **2009,** *5* (6), 666-671.
5. Crawford, R. J.; Webb, H. K.; Truong, V. K.; Hasan, J.; Ivanova, E. P. Surface topographical factors influencing bacterial attachment. *Advances in Colloid and Interface Science* **2012,** *179-182*, 142-149.
6. Elter, P.; Lange, R.; Beck, U. Atomic force microscopy studies of the influence of convex and concave nanostructures on the adsorption of fibronectin. *Colloids and Surfaces B: Biointerfaces* **2012,** *89*, 139-146.
7. Messina, G. M. L.; Bocchinfuso, G.; Giamblanco, N.; Mazzuca, C.; Palleschi, A.; Marletta, G. Orienting proteins by nanostructured surfaces: evidence of a curvature-driven geometrical resonance. *Nanoscale* **2018,** *10* (16), 7544-7555.
8. Grigorescu, A. E.; Hagen, C. W. Resists for sub-20-nm electron beam lithography with a focus on HSQ: state of the art. *Nanotechnology* **2009,** *20* (29), 292001.
9. Gentile, F.; Tirinato, L.; Battista, E.; Causa, F.; Liberale, C.; di Fabrizio, E. M.; Decuzzi, P. Cells preferentially grow on rough substrates. *Biomaterials* **2010,** *31* (28), 7205-7212.
10. Lipski, A. M.; Jaquiery, C.; Choi, H.; Eberli, D.; Stevens, M.; Martin, I.; Chen, I. W.; Shastri, V. P. Nanoscale Engineering of Biomaterial Surfaces. *Advanced Materials* **2007,** *19* (4), 553-557.
11. Scopelliti, P. E.; Borgonovo, A.; Indrieri, M.; Giorgetti, L.; Bongiorno, G.; Carbone, R.; Podestà, A.; Milani, P. The Effect of Surface Nanometre-Scale Morphology on Protein Adsorption. *PLoS ONE* **2010,** *5* (7), e11862.
12. Dolatshahi-Pirouz, A.; Hovgaard, M. B.; Rechendorff, K.; Chevallier, J.; Foss, M.; Besenbacher, F. Scaling behavior of the surface roughness of platinum films grown by oblique angle deposition. *Physical Review B* **2008,** *77* (11), 115427.
13. Backholm, M.; Foss, M.; Nordlund, K. Roughness of glancing angle deposited titanium thin films: an experimental and computational study. *Nanotechnology* **2012,** *23* (38), 385708.
14. Liascukiene, I.; El Kirat, K.; Beauvais, M.; Asadauskas, S. J.; Lambert, J.-F.; Landoulsi, J. Lipid Layers on Nanoscale Surface Topography: Stability and Effect on Protein Adsorption. *Langmuir* **2017,** *33* (18), 4414-4425.
15. Zhang, J.; Huang, J.; Say, C.; Dorit, R. L.; Queeney, K. T. Deconvoluting the effects of surface chemistry and nanoscale topography: Pseudomonas aeruginosa biofilm nucleation on Si-based substrates. *Journal of Colloid and Interface Science* **2018,** *519*, 203-213.
16. Kessenich, B. L.; Pokhrel, N.; Nakouzi, E.; Newcomb, C. J.; Flury, M.; Maibaum, L.; De Yoreo, J. J. Connecting wettability, topography, and chemistry in a simple lipid-montmorillonite system. *Journal of Colloid and Interface Science* **2019,** *555*, 498-508.
17. Whitehouse, D. J. *Handbook of surface metrology*; IOP Publishing Ltd1994.
18. Wieland, M.; Hänggi, P.; Hotz, W.; Textor, M.; Keller, B. A.; Spencer, N. D. Wavelength-dependent measurement and evaluation of surface topographies: application of a new concept of window roughness and surface transfer function. *Wear* **2000,** *237* (2), 231-252.
19. Gong, Y.; Misture, S. T.; Gao, P.; Mellott, N. P. Surface Roughness Measurements Using Power Spectrum Density Analysis with Enhanced Spatial Correlation Length. *The Journal of Physical Chemistry C* **2016,** *120* (39), 22358-22364.

20. González Martínez, J. F.; Nieto-Carvajal, I.; Abad, J.; Colchero, J. Nanoscale measurement of the power spectral density of surface roughness: how to solve a difficult experimental challenge. *Nanoscale Res Lett* **2012,** *7* (1), 174.
21. Angela Duparré; Josep Ferre-Borrull; Stefan Gliech, G. N.; Jörg Steinert; Jean M. Bennett. Surface characterization techniques for determining the root-mean-square roughness and power spectral densities of optical components. *Appl. Opt.* **2002,** *41*, 154-171.
22. Sarkar, S.; Patra, S.; Gayathri, N.; Banerjee, S. Effect of self-affine fractal characteristics of surfaces on wetting. *Applied Physics Letters* **2010,** *96* (6), 063112.
23. Goovaerts, P. *Geostatistics for natural resources evaluation*; Oxford University Press: New York, 1997.
24. Chilès, J.-P.; Pierre Delfiner. *Geostatistics modeling spatial uncertainty*; Wiley: New York, 1999.
25. Liascukiene, I.; Aissaoui, N.; Asadauskas, S. J.; Landoulsi, J.; Lambert, J.-F. Ordered Nanostructures on a Hydroxylated Aluminum Surface through the Self-Assembly of Fatty Acids. *Langmuir* **2012,** *28* (11), 5116-5124.
26. Liascukiene, I.; Steffenhagen, M.; Asadauskas, S. J.; Lambert, J.-F.; Landoulsi, J. Self-Assembly of Fatty Acids on Hydroxylated Al Surface and Effects of Their Stability on Wettability and Nanoscale Organization. *Langmuir* **2014,** *30* (20), 5797-5807.
27. Landoulsi, J.; Dupres, V. Direct AFM force mapping of surface nanoscale organization and protein adsorption on an aluminum substrate. *Physical Chemistry Chemical Physics* **2013,** *15* (21), 8429-8440.
28. https://cran.r-project.org/web/packages/AFM/index.html.
29. Barabási, A. L.; Stanley, H. E. *Fractal Concepts in Surface Growth*; Cambridge University Press: Cambridge, 1995.
30. Foadi, F.; Vaez Allaei, S. M.; Palasantzas, G.; Mohammadizadeh, M. R. Roughness-dependent wetting behavior of vapor-deposited metallic thin films. *Physical Review E* **2019,** *100* (2), 022804.
31. Rechendorff, K.; Hovgaard, M. B.; Chevallier, J.; Foss, M.; Besenbacher, F. Tantalum films with well-controlled roughness grown by oblique incidence deposition. *Applied Physics Letters* **2005,** *87* (7), 073105.
32. Silk, T.; Hong, Q.; Tamm, J.; Compton, R. G. AFM studies of polypyrrole film surface morphology II. Roughness characterization by the fractal dimension analysis. *Synthetic Metals* **1998,** *93* (1), 65-71.
33. Krim, J.; Indekeu, J. O. Roughness exponents: A paradox resolved. *Physical Review E* **1993,** *48* (2), 1576-1578.
34. Family, F. Dynamic scaling in surface growth: theory, simulations and experiments. In *Conference on dynamical phenomena at interfaces, surfaces and membranes*, D. Beysens, G. F., N. Boccara, Ed.: Les Houches, France, 1991.
35. Klinkenberg, B. A review of methods used to determine the fractal dimension of linear features. *Mathematical Geology* **1994,** *26* (1), 23-46.
36. Sidick, E. *Power spectral density specification and analysis of large optical surfaces*; SPIE2009; Vol. 7390.
37. Viville, P.; Lazzaroni, R.; Brédas, J. L.; Moretti, P.; Samorí, P.; Biscarini, F. The Influence of Thermal Annealing on the Morphology of Sexithienyl Thin Films. *Advanced Materials* **1998,** *10* (1), 57-60.
38. Olea, R. A. A six-step practical approach to semivariogram modeling. *Stoch Environ Res Ris Assess* **2006,** *20* (5), 307-318.
39. Coburn, T. C.; Yarus, J. M.; Chambers, R. L. *Stochastic modeling and geostatistics: Principles, methods and case studies*; The American Asociation of Petroleum Geologists: Oklahoma, 2006; Vol. 2.
40. Bailly, J.-S.; Le Coarer, Y.; Languille, P.; Stigermark, C.-J.; Allouis, T. Geostatistical estimations of bathymetric LiDAR errors on rivers. *Earth Surface Processes and Landforms* **2010,** *35* (10), 1199-1210.
41. Cressie, N.; Hawkins, D. M. Robust estimation of the variogram: I. *Journal of the International Association for Mathematical Geology* **1980,** *12* (2), 115-125.

42. Pfeifer, P. Fractal dimension as working tool for surface-roughness problems. *Applications of Surface Science* **1984,** *18* (1), 146-164.
43. Davies, S.; Hall, P. Fractal analysis of surface roughness by using spatial data. *Journal of the Royal Statistical Society: Series B (Statistical Methodology)* **1999,** *61* (1), 3-37.
44. Baker, B. R.; Pearson, R. M. Water content of pseudoboehmite: A new model for its structure. *Journal of Catalysis* **1974,** *33* (2), 265-278.
45. van den Brand, J.; Blajiev, O.; Beentjes, P. C. J.; Terryn, H.; de Wit, J. H. W. Interaction of Ester Functional Groups with Aluminum Oxide Surfaces Studied Using Infrared Reflection Absorption Spectroscopy. *Langmuir* **2004,** *20* (15), 6318-6326.
46. Barnes, R. J. The variogram sill and the sample variance. *Mathematical Geology* **1991,** *23*, 673–678.
47. Landoulsi, J.; Genet, M. J.; Fleith, S.; Touré, Y.; Liascukiene, I.; Méthivier, C.; Rouxhet, P. G. Organic adlayer on inorganic materials: XPS analysis selectivity to cope with adventitious contamination. *Applied Surface Science* **2016,** *383*, 71-83.
48. Methivier, C.; Lebec, V.; Landoulsi, J.; Pradier, C. M. Probing the Binding Mechanism of Peptides on a Copper Surface: Multilayer Self-Assembly Promoted by Glutamate Residues. *The Journal of Physical Chemistry C* **2011,** *115* (10), 4041-4046.
49. Venables, W. N.; Ripley, B. D. *Modern Applied Statistics with S*; Springer2002.
50. de Gennes, P.-G.; Brochard-Wyart, F.; Quere, D. *Capillarity and Wetting Phenomena. Drops, Bubbles, Pearls, Waves*; Springer: New York, 2004.
51. Jonas, A. M.; Cai, R.; Vermeyen, R.; Nysten, B.; Vanneste, M.; De Smet, D.; Glinel, K. How roughness controls the water repellency of woven fabrics. *Materials & Design* **2020,** *187*, 108389.

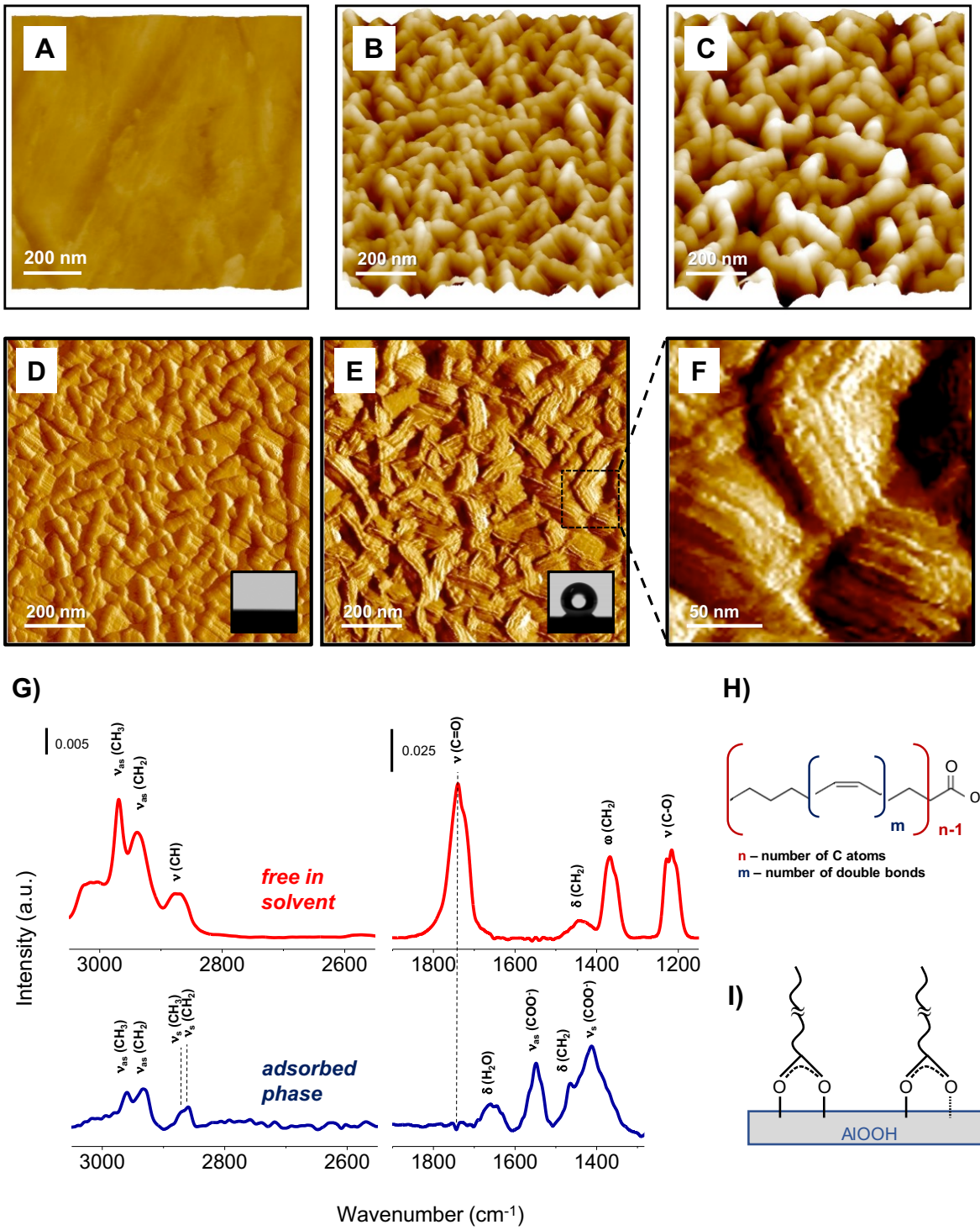

Figure 1.(A-C) Representative AFM height images (1 × 1 μm^2, peak force tapping mode, *z*-scale 130 nm) recorded on aluminum substrate (A, *Al*) prior to or (B, *Al-nano*) after hydroxylation treatment in boiling water and (C, *Al-nano_Ox*) further incubation in hydrogen peroxide solution (H_2O_2, 10 mM). (D, E, F) Representative AFM deflection images (1 × 1 μm^2, peak force tapping mode) recorded on hydroxylated aluminum before (D) and after (E) the adsorption of oleic acid (*Al-nano_OA*). Image (F) is a zoom taken at the location indicated by dashed lines

in image (E). (G) IR-ATR (top, red line) spectrum recorded in solution of oleic acid (in heptane) and PM-IRRAS (bottom, blue line) spectrum recorded on *Al-nano* substrate after adsorption of oleic acid. (H) Molecular structure of fatty acids (FAs). (I) Examples of possible binding modes of FAs to the hydroxylated aluminum surface.

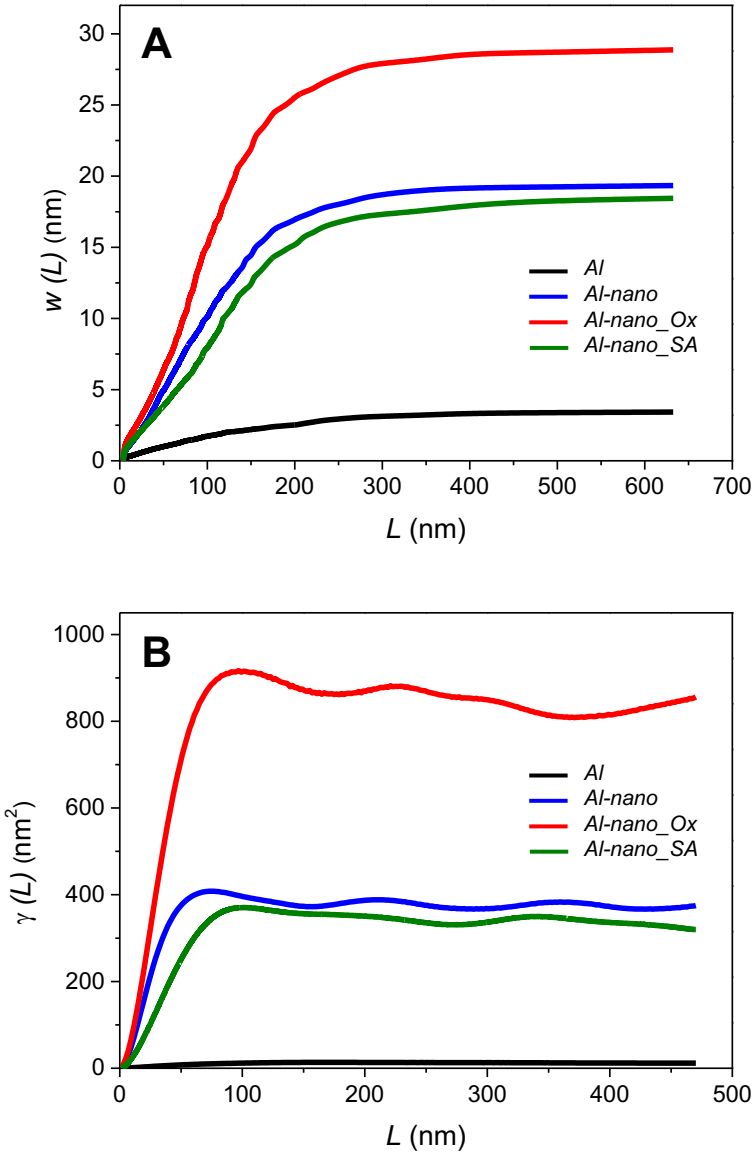

Figure 2. (A) *w* (*L*) *vs L* plots constructed from PSD analysis and (B) semi-variograms of AFM images recorded on: (A) aluminum substrate prior to (*Al*) or after hydroxylation treatment in boiling water (*Al-nano*) and further incubation in hydrogen peroxide solution (*Al-nano_Ox*), or on *Al-nano* surface modified with stearic acid (*Al-nano_SA*).

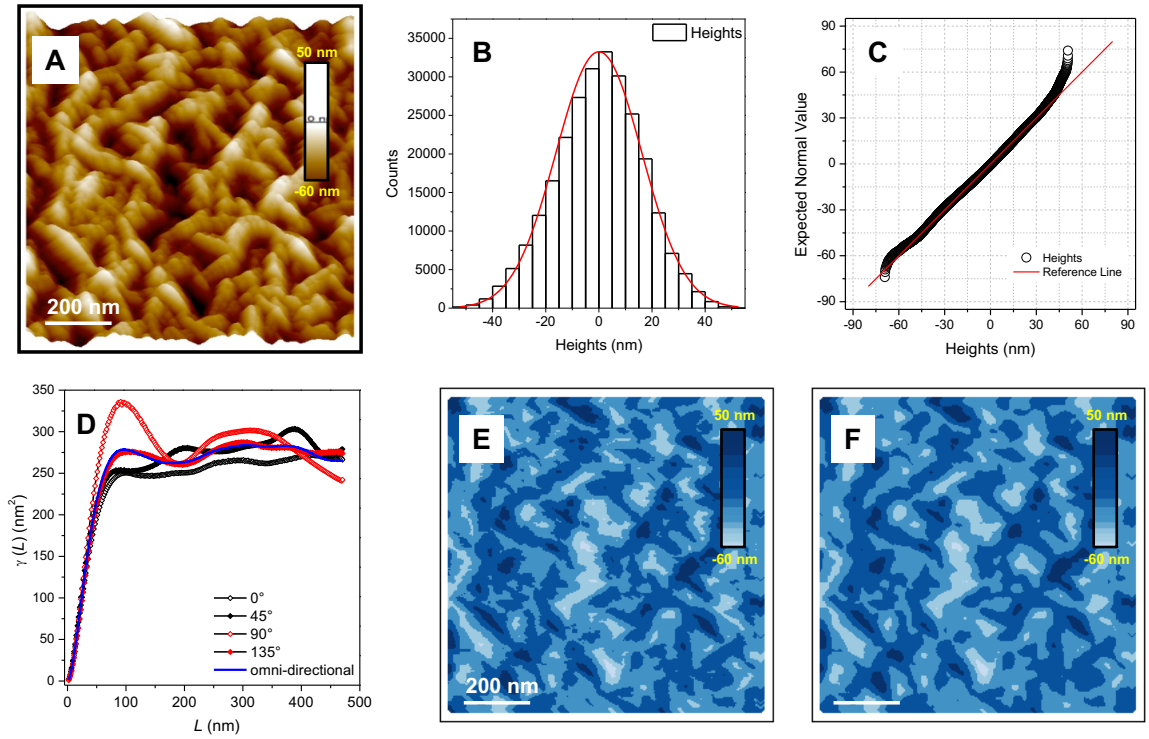

Figure 3. Procedure used for experimental variogram calculation and variogram modeling. (A) Representative AFM height image recorded on the nanostructured aluminum substrate (*Al-nano*). (B) Visualizations of the distribution of heights to check the normality of the heights. (C) Quantile-Quantile plot showing the correlation between the sample heights and the normal distribution. (D) Directional variograms to check isotropy of the sample. (E, F) Comparative visualization of the (E) real and (F) predicted heights of the sample surface.

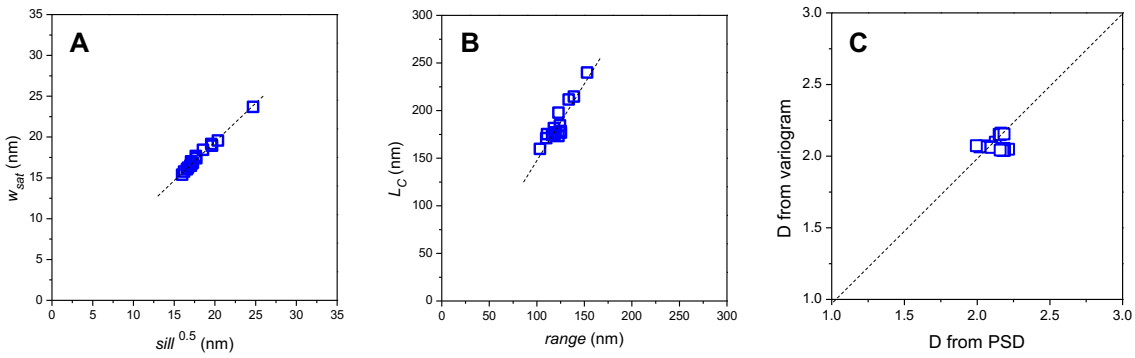

Figure 4. Correlations between (A) w_{sat} (PSD calculation) and the square root of *sill* (theoretical variogram calculation), (B) L_c (PSD calculation) and *range* (theoretical variogram calculation), and (C) fractal dimensions computed from PSD or variogram calculations. The different parameters are calculated from AFM images recorded on nanostructured aluminum samples modified with fatty acids. Dashed lines correspond to the regression lines: (A) y = 0.93x + 0.74 (adjusted R^2 = 0.99, p-value= 6.354e-15), (B) y = 1.60x – 11.23 (adjusted R^2 = 0.84, p-value= 3.219e-07), (C) y = x.

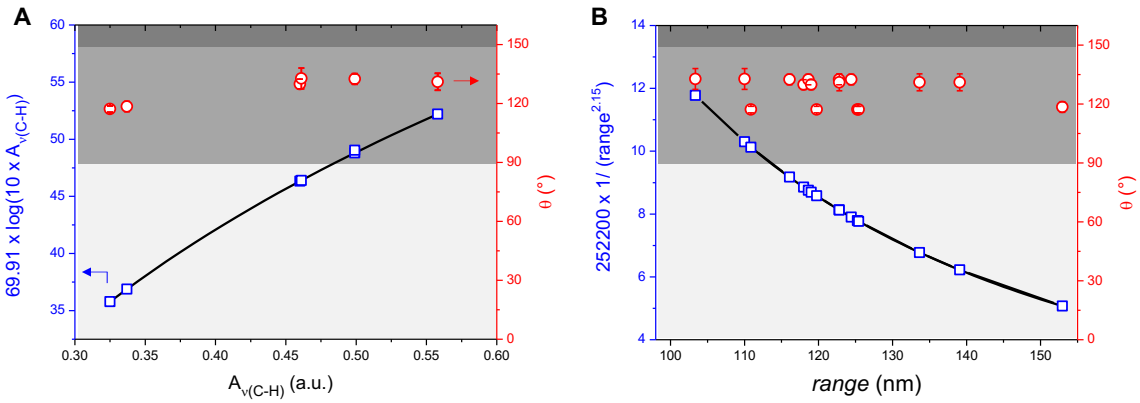

Figure 5. Contributions of (A) $A_{v(C-H)}$ and (B) *range* to the terms due to "chemistry" and "roughness", respectively, used to calculate water contact angle, θ_w : (left y-axis) open squares (☐) correspond to values of boxed variables and line corresponds to the mathematical function used for the variable transformation (Box-Cox transformation, see Supporting information for more details); (right y-axis) open circles are experimental θ_w values measured on the different *Al-nano_FA* samples. Both graphs (A and B) include the same number of samples (n = 16), some points are overlapping in panel A. Gray area gradients correspond to different wetting properties commonly termed, from bright to dark: hydrophilic, hydrophobic, superhydrophobic.

Graphical abstract

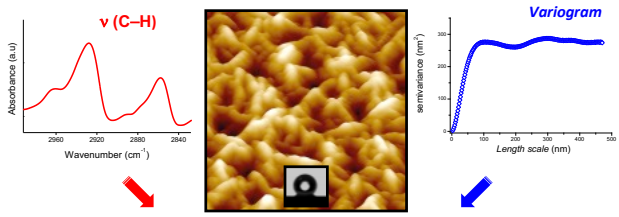

$$\theta_w = A + B \times log\left(10 \times A_{\nu(C-H)}\right) + C \times \frac{1}{range^{2.15}}$$